Applied Surface Science 521 (2020) 146389

Contents lists available at ScienceDirect

Applied Surface Science

journal homepage: www.elsevier.com/locate/apsusc

Improved electrochemical performances and magnetic properties of lithium iron phosphate with *in situ* Fe_2P surface modification by the control of the reductive gas flow rate

Wenyu Yang[a,b], Lin Zhang[a,c], Yue Chen[a,c], Hurong Yao[a,d], Jiaxin Li[a,d], Yingbin Lin[a,c], Zhigao Huang[a,d,*]

[a] College of Physics and Energy, Fujian Normal University, Fujian Provincial Key Laboratory of Quantum Manipulation and New Energy Materials, Fuzhou 350117, China
[b] College of Mathematics and Physics, Ningde Normal University, Ningde 352100, China
[c] Fujian Provincial Engineering Technical Research Centre of Solar-Energy Conversion and Stored Energy, Fuzhou 350117, China
[d] Fujian Provincial Collaborative Innovation Center for Optoelectronic Semiconductors and Efficient Devices, Xiamen 361005, China

ARTICLE INFO

Keywords:
Lithium iron phosphate
Electrochemical performance
Iron phosphide
Surface modification
Magnetic property

ABSTRACT

The growth of Fe_2P was successfully regulated in the inner surface of $LiFePO_4$ by the control of the reductive gas flow rate. The as-synthesized composites were characterized by XRD, XPS, TEM, and magnetic measurements. The experimental results indicated that the Fe_2P content of the samples increases with the increasing reductive gas flow rate. Moreover, due to the effective conductive path from Fe_2P, it was found that the moderate modified-Fe_2P $LiFePO_4$ sample had an excellent rate performance and cyclic stability under a high current density. It was also confirmed that $LiFePO_4$ decorated with a moderate amount of Fe_2P shows a lower charge transfer resistance and higher Li^+ diffusion coefficient than that of the other samples examined in our investigation. However, excessive Fe_2P modification had a negative effect on the enhancement of the electrochemical performance, which was mainly attributed to the large amount of available Fe_2P; its non-electrochemical activity sacrifices the specific capacity of the $LiFePO_4$ material. This work provides a novel method to obtain high performance by controlling the gas flow rate to optimize the amount of conducting Fe_2P. Furthermore, the potential relationship between the $LiFePO_4$ material's electrochemical and magnetic properties was investigated. It was believed that the magnetic moment is a simple and sensitive method for detecting the electrochemical performances of $LiFePO_4$ electrode materials.

1. Introduction

Lithium iron phosphate ($LiFePO_4$) is an important cathode material used for lithium ion batteries because of its excellent safety performance and long cycle life [1,2]. It is widely used in many applications, such as cell phone batteries, energy storage power stations in large shopping malls, and power storage systems for electric buses [3,4]. However, this material still has some problems that need to be solved. Because of the poor electronic and ionic conductivity induced by the intrinsic properties of the material [5], the specific capacity of batteries and their capacity retention are unsatisfying, especially at a high current density. Many strategies have been adopted to ensure that each active particle is provided with a high conductivity to effectively facilitate electron and lithium ion transportation in the electrode, such as the application of an amorphous carbon coating [6,7] and ion doping [8,9]. The amorphous carbon coating on the surface of a particle not only acts as a fast channel for electron transport but also (more importantly) blocks the liquid electrolyte from penetrating into the active material's interior and consequently alleviates the solid-liquid interfacial reaction, which enables an excellent cycle stability of the $LiFePO_4$ cathode. Ion doping, like carbon modification, can reinforce the lattice structures of materials and enhance electrical conductivity.

Selecting an iron phosphide (Fe_2P) compound as the surface modification layer of a material is an effective approach to further enhance the rate performance of a $LiFePO_4$ cathode at a high current density. This is because the Fe_2P compound has an excellent electrical conductivity at room temperature. The carbon coating, sintering temperature, sintering time, and reducing atmosphere are the main factors

* Corresponding author at: College of Physics and Energy, Fujian Normal University, Fujian Provincial Key Laboratory of Quantum Manipulation and New Energy Materials, Fuzhou 350117, China.
E-mail address: zghuang@fjnu.edu.cn (Z. Huang).

https://doi.org/10.1016/j.apsusc.2020.146389
Received 28 October 2019; Received in revised form 24 March 2020; Accepted 19 April 2020
Available online 21 April 2020
0169-4332/

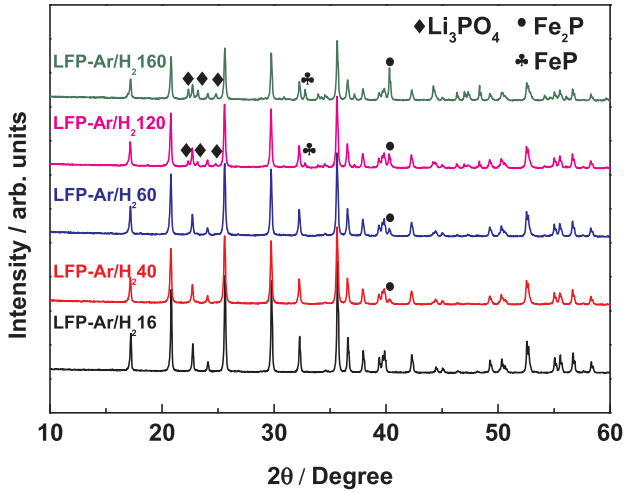

Fig. 1. XRD patterns of LFP-AH16, LFP-AH40, LFP-AH60, LFP-AH120, and LFP-AH160.

that contribute to the growth of Fe_2P on a particle's surface [10,11]. There were some studies on modifying the $LiFePO_4$ cathode material with a Fe_2P conductive substance [12–15]. For example, Yin et al. [12] successfully synthetized Fe_2P and FeP composites on the surface of lithium iron phosphate particles using a high-temperature solid-state method. As a result, the tap density of the material increased and its specific capacity was dramatically enhanced (up to 100 $mAhg^{-1}$ at a current density of 10 C). Rahman et al. [14] reported that when ferromagnetic Fe_2P was decorated on the surface of antiferromagnetic $LiFePO_4$, it created a strong interface coupling effect between the two substances (the "exchange bias" effect). This effect directly reduces the electron transfer resistance within the electrode, consequently enhancing the specific capacity of the material. However, most of the investigations focused on the improvement in the electrochemical performance of $LiFePO_4$ through controlling the carbon coating content and sintering temperature. The literature also lacks an evaluation of the relationship between the magnetic properties and the electrochemical performance of $LiFePO_4$ materials. Interestingly, in addition to the influencing factors noted above, the velocity of the reducing atmosphere (Ar/H_2) has a big impact on the formation of Fe_2P compounds. As far as we know, there are few studies that examine this impact.

The mesoscopic-sized Fe_2P compound on the surface of $LiFePO_4$ was fabricated *in situ* by adjusting the reductive gas flow rate. It was needed to tailor the reducing atmosphere flow rate for the optimization of the material's electrochemical behavior. The experimental results revealed that the appropriate Fe_2P surface modification can induce a dramatically improved rate performance and cycling stability of the material's cathode. Combined with the results of the electrochemical testing, the detailed structural and morphological characterization indicate that the content of the Fe_2P production is proportional to the flow rate of the reductive gas. Unlike the residual amorphous carbon that adhered to the outer surface of the particles, the Fe_2P compound was located on the inner surface of $LiFePO_4$. Fe_2P provided a faster transfer channel for electrons and later improved the electrochemical kinetic behavior of the as-synthetized composite. Through the employment of different reductive gas flow rates, we easily realized controllable Fe_2P growth on the surface of $LiFePO_4$. It was distinct from the earlier study, where the controlled growth of Fe_2P required cumbersome crafting and high-energy consumption. The *in situ* mesoscopic size decoration of Fe_2P on the surface of $LiFePO_4$ at 700 °C was simply accomplished by adjusting the reductive gas flow rate rather than using the complicated carbon content control approach. This work provides insight into how the reductive gas flow rate can affect the magnetic and electrochemical

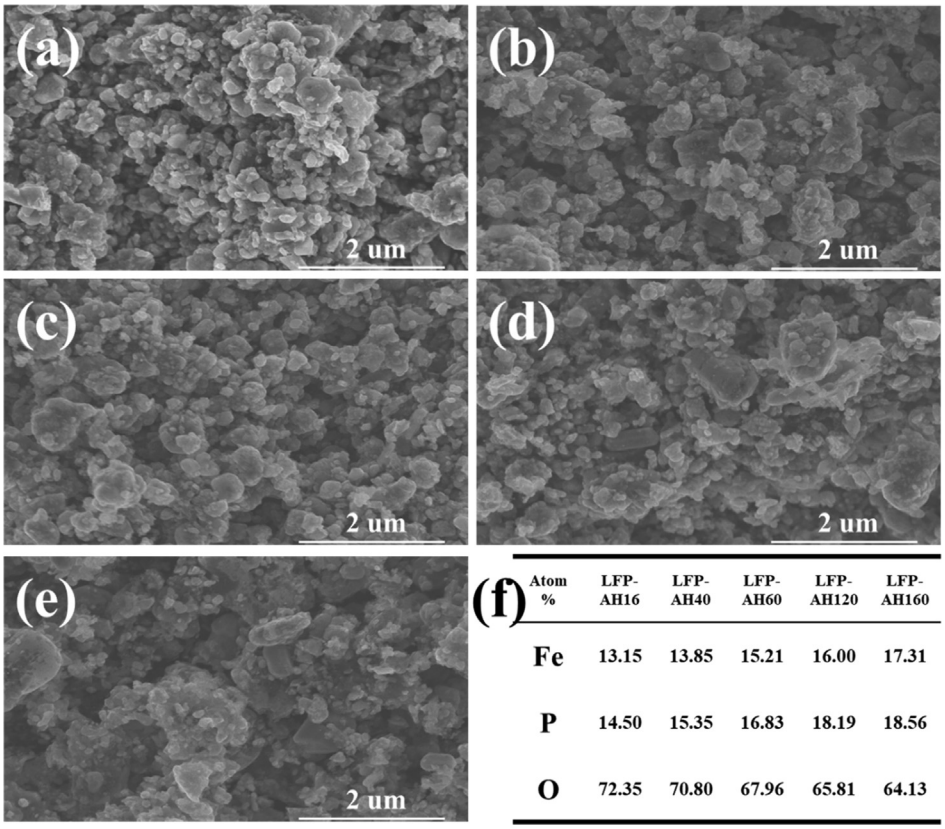

(f)

Atom %	LFP-AH16	LFP-AH40	LFP-AH60	LFP-AH120	LFP-AH160
Fe	13.15	13.85	15.21	16.00	17.31
P	14.50	15.35	16.83	18.19	18.56
O	72.35	70.80	67.96	65.81	64.13

Fig. 2. Morphologies of the samples with (a) LFP-AH16, (b) LFP-AH40, (c) LFP-AH60, (d) LFP-AH120, and (e) LFP-AH160; (f) distribution ratio of each element for five samples.

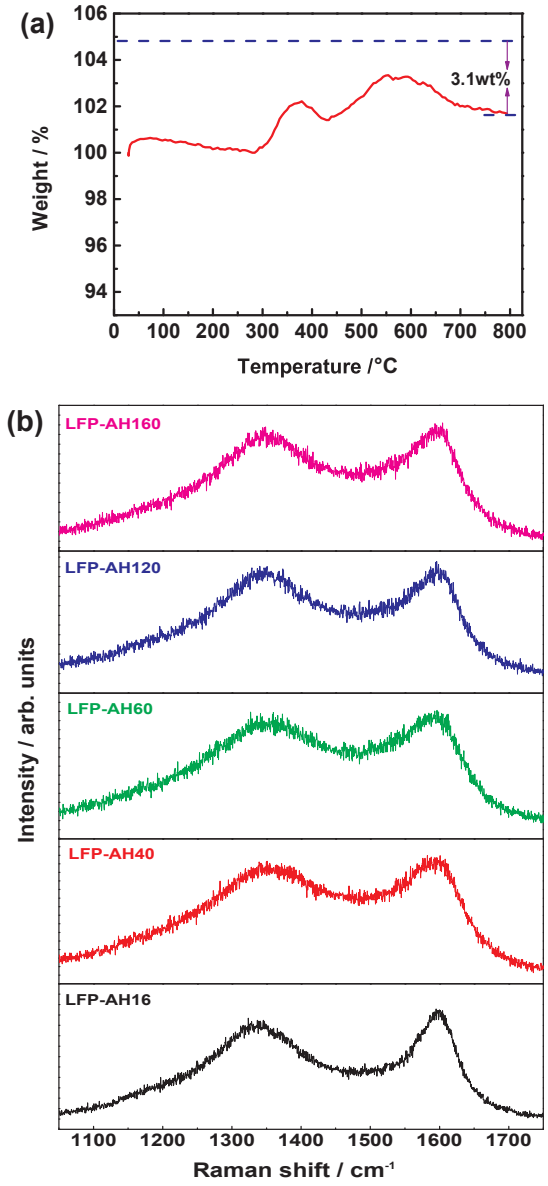

Fig. 3. (a) Thermogravimetric curve of $LiFePO_4$ material; (b) Raman spectra of LFP-AH16, LFP-AH40, LFP-AH60, LFP-AH120, and LFP-AH160.

performances of materials and offers guidance for the design of polyanionic electrode material preparation.

2. Experimental

2.1. Preparation of material

The $LiFePO_4$ powders were synthesized using a solid-state reaction route, where $C_2H_3O_2Li{\cdot}2H_2O$, $FeC_2O_4{\cdot}2H_2O$, and $NH_4H_2PO_4$ were used as starting materials with a nonstoichiometric molar ratio of 1.02:1:1, and 5 wt% sucrose ($C_{12}H_{22}O_{11}$) was added as a reducing agent and carbon source. First, the mixture materials were dispersed in acetone, and then were milled for 48 h with a rotation speed of 400 rpm. To remove excess acetone, the resultant product was dried in an oven at 60 °C. Subsequently, the dried mixtures were pre-treated by heating at 350 °C for 6 h and then calcined at 700 °C for 12 h under a shielding gas. The protective and reducing gas consisted of 95% Ar and 5% H_2.

The same heat treatment procedure was adopted for the preparation of $LiFePO_4/Fe_2P/C$, where the mixed gas flow rates of 16, 40, 60, 120, and 160 mL/min were applied; the obtained samples were marked as LFP-AH16, LFP-AH40, LFP-AH60, LFP-AH120, and LFP-AH160, respectively. A heating rate of 3 °C min^{-1} and natural cooling were used in the calcination process.

2.2. Characterization of the material and cell fabrication

The crystalline phase of the synthesized samples was identified by powder x-ray diffraction (XRD) with Cu K_α radiation (λ = 0.15406 nm). The morphologies of the powders were observed with a scanning electron microscope (SEM, Hitachi SU8010) using energy dispersive spectroscopy (EDS). The amount of carbon in the powder sample was obtained by a thermogravimetric analyzer (Netzsch STA409PC TA instrument) at a scanning rate of 5 °C min^{-1} with an air flow of 40 mL min^{-1} from room temperature to 800 °C. The chemical valence states of the as-prepared composites were analyzed by x-ray photoelectron spectroscopy (XPS, Thermo Fisher ESCALAB 250Xi) with an Al-K_α (1486.6 eV) excitation source. The Raman technique (Bruker SENTERRA with 532 nm laser excitation) was used to obtain the spectra of the samples' surface. Magnetization measurements were performed with a VSM (LakeShore EM7037/9509-P, USA), and the investigation was conducted at 300 K on freeze-dried samples with applied magnetic fields up to 0.9 T. The electrochemical measurements were carried out using an assembly of 2025 coin-type cells, where the lithium metal was treated as the anode and lithium iron phosphate was used as the cathode. The work electrode was made by mixing the active material, Super P, and polyvinylidene fluoride (PVDF) in a weight ratio of 8:1:1. The electrolyte was 1 M $LiPF_6$ in EC/DMC (1/1) solution. All cells were assembled in an Ar-filled glove box. For the cycling test, the batteries were charged at 10 C to 4.3 V and then discharged to 2.5 V at 10 C. The rate performance evaluation of the sample was implemented at various current densities. The electrochemical impedance spectroscopy (EIS) was carried out in a frequency range from 10 mHz to 100 kHz with an AC signal of 5 mV. All tests were performed at room temperature.

3. Results and discussion

The XRD patterns of the as-prepared samples are shown in Fig. 1. The main diffraction peaks of the samples are in accordance with orthorhombic $LiFePO_4$ (JCPDS Card No. 40-1499, space group *Pmnb*(62), a = 6.018 Å, b = 10.347 Å, c = 4.703 Å) [16]. Evidently, there is a weak peak at 40.1° for sample LFP-AH40 besides the typical $LiFePO_4$ peaks, which is indexed to the Fe_2P phase [17,18]. Fe_2P has a high-electronic conductivity of 10^{-1} S cm^{-1} [19]. It was suggested that the formation of Fe_2P at the grain boundaries of $LiFePO_4$ can demonstrate a remarkable increase of the electronic conductivity of $LiFePO_4$ materials [20]. Furthermore, it can be seen that the amount of Fe_2P increases with the gas flow rate by comparing the test results. When the gas flow rate is up to 120 mL/min or 160 mL/min, a considerable amount of Li_3PO_4 and FeP impurities appear in the final product.

The morphologies of the $LiFePO_4$ calcined at different gas flow rates are shown in Fig. 2(a) – (e), respectively. The SEM images illustrate that the particle size and morphologies of the $LiFePO_4$ material have no major changes, even at different gas flow rates. All samples display a homogeneous size in the range from 1 μm to 2 μm. Moreover, Figs. 1 and 2 show that the increase of the gas flow rate can effectively contribute to the formation of Fe_2P, while the morphologies of the $LiFePO_4$ material mainly do not change. The content of the residual carbon on the surface of materials was confirmed by thermogravimetric analysis. As shown in Fig. 3(a), the residual carbon content in the final product is about 3.1 wt%. Covering the surface of particles with residual carbon is conducive to suppressing the overgrowth of the $LiFePO_4$ particle size, which plays a significant role in enhancing the electrical conductivity and lithium ion diffusion [21,22]. Fig. 2(f) displays the distribution ratio of each element for samples LFP-AH16, LFP-AH40, LFP-AH60, LFP-AH120, and LFP-AH160. Compared to LFP-AH16, LFP-AH160

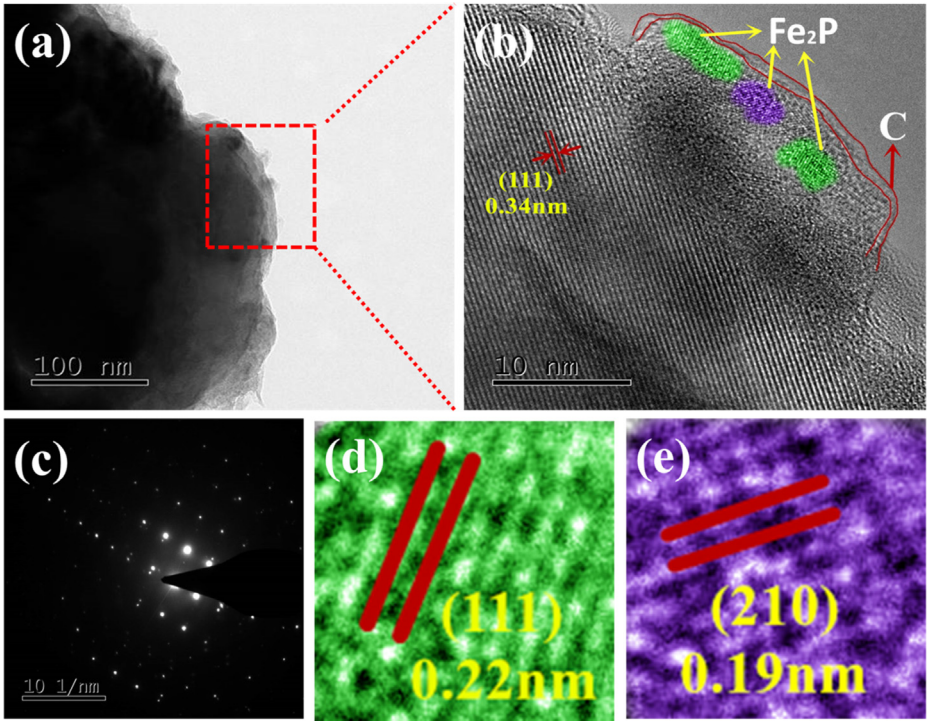

Fig. 4. (a) TEM image of LFP-AH40, (b) area enlargement of a TEM picture of LFP-AH40, (c) electron diffraction (SAED) pattern of the selected area, (d) (1 1 1) and (e) (2 1 0) crystallographic planes of Fe_2P.

shows more Fe-rich and P-rich regions, indicating the presence of more Fe_2P.

The Raman spectra of LFP-AH16, LFP-AH40, LFP-AH60, LFP-AH120, and LFP-AH160 shown in Fig. 3(b) were used to evaluate the structural properties of the residual carbon coating on the surface of composite material. The two main double peaks observed at 1339.2 cm^{-1} and 1598.5 cm^{-1} are assigned to the *D*-band (*K*-point phonons of A_{1g} symmetry) and *G*-band (E_{2g} phonons of *C* sp^2 atoms), respectively [23]. The *G*-band is associated with the existence of graphite carbon, whereas the *D*-band is attributed to disorders or defects in the graphite structure. The intensity ratio between the *D* peak and *G* peak can be used to determine the graphitization degree of the carbon material. By comparison, the Raman peak intensity ratio of each sample has no evident difference, implying that the as-prepared samples have a similar carbon structure.

For deeper insights into the microstructure of the composite materials, the TEM images of the LFP-AH40 were evaluated, as shown in Fig. 4(a) and (b). The lattice fringe of $LiFePO_4$ is clearly distinguished in the magnification of the local area. Its interplanar distance is 0.34 nm, corresponding to a (1 1 1) crystallographic plane. A layer of amorphous carbon with a thickness of about 2 nm is observed on the surface of $LiFePO_4$ particle. In addition, the electron diffraction (SAED) pattern in the selected area of the sample exhibits distinct diffraction spots, revealing the $LiFePO_4$ particle is characteristic of a single crystal. In the inner part of the $LiFePO_4$ particle surface, the spacings of the lattice fringe are 0.22 nm and 0.19 nm, respectively. They correspond to the (1 1 1) and (2 1 0) crystallographic planes of the conductive phase Fe_2P, respectively (marked with green and purple). The formation of these nano Fe_2P particles is mainly due to the inner surface of $LiFePO_4$ being reduced via the cooperation of the reductive gas and carbon coating.

The XPS technique is a suitable characterization tool for investigating the chemical valence state of the material. Due to the spin-orbit coupling, the Fe2p spectrum displayed in Fig. 5(a) splits into two peaks at 710.2 (Fe2p3/2) (marked as peak 2) and 723.0 eV (Fe2p1/2) (marked as peak 4), and is accompanied with the corresponding satellite peaks at 713.5 (marked as peak 3) and 727.0 eV (marked as peak 5), which is consistent with the observed spectra of the $LiFePO_4$ [24,25]. Moreover, Fig. 5(b) – (e) shows that the intensity of the peak at 707.4 eV (marked as peak 1) corresponds to the phase of Fe_2P [10], and it is being gradually enhanced with the increasing reductive gas flow rate. By calculating the peak area ratio of Fe_2P (707.4 eV) and $LiFePO_4$ (including Fe2p3/2 (710.2 eV) and Fe2p1/2 (723.0 eV)), the content of Fe_2P in LFP-AH40, LFP-AH60, LFP-AH120 and LFP-AH160 were identified. The calculated results indicated that the ratios of the Fe_2P phase generated on the surface of samples LFP-AH40, LFP-AH60, LFP-AH120, and LFP-AH160 are about 2.62 wt%, 3.19 wt%, 4.13 wt%, and 9.55 wt %, respectively. Moreover, notable changes are also observed in the P2p spectra with the increasing reductive gas flow rate. As shown in Fig. 5(f) – (j), the peaks located at 133.0 eV and 134.0 eV correspond to phosphate. The peaks at 128.5 eV and 130.1 eV belong to phosphide. The intensity of the peaks related to phosphide is evidently enhanced with the increasing gas flow rate, indicating the increased content of Fe_2P. This is consistent with the result in Fig. 1.

Fig. 6(a) exhibits the charge–discharge profile of LFP-AH16, LFP-AH40, LFP-AH 60, LFP-AH120, and LFP-AH160 at 0.2 C (1 C = 170 $mAhg^{-1}$). When the samples were tested at a low current density, the charge/discharge curves showed flat plateaus around 3.48 V vs. Li/Li^+, which corresponds to the characteristic charge/discharge work voltage of $LiFePO_4$. The discharge capacities for LFP-AH16, LFP-AH40, LFP-AH60, LFP-AH120, and LFP-AH160 are 149.8, 155.8, 141.9, 100.7, and 96.2 $mAhg^{-1}$, respectively. These results were attributed to the low density current, and the polarization phenomenon of the samples was not prominent. In comparison with the other samples, LFP-AH40 displays an enhanced capacity due to the involvement of the Fe_2P conductive phase. However, the modified $LiFePO_4$ exhibits a considerable loss of capacity with the further increase of the Fe_2P content. Excessive Fe_2P modification has a negative effect on the enhancement of $LiFePO_4$'s electrochemical performance.

Fig. 6(b) shows the rate capability of LFP-AH16, LFP-AH40, LFP-AH60, LFP-AH120, and LFP-AH160 at room temperature. The rate capacity of LFP-AH40 reaches 155.8, 152.3, 144.9, 137.1, 124.9, and 115 $mAhg^{-1}$ at 0.2 C, 0.5 C, 1 C, 2 C, 5 C, and 10 C, respectively. By

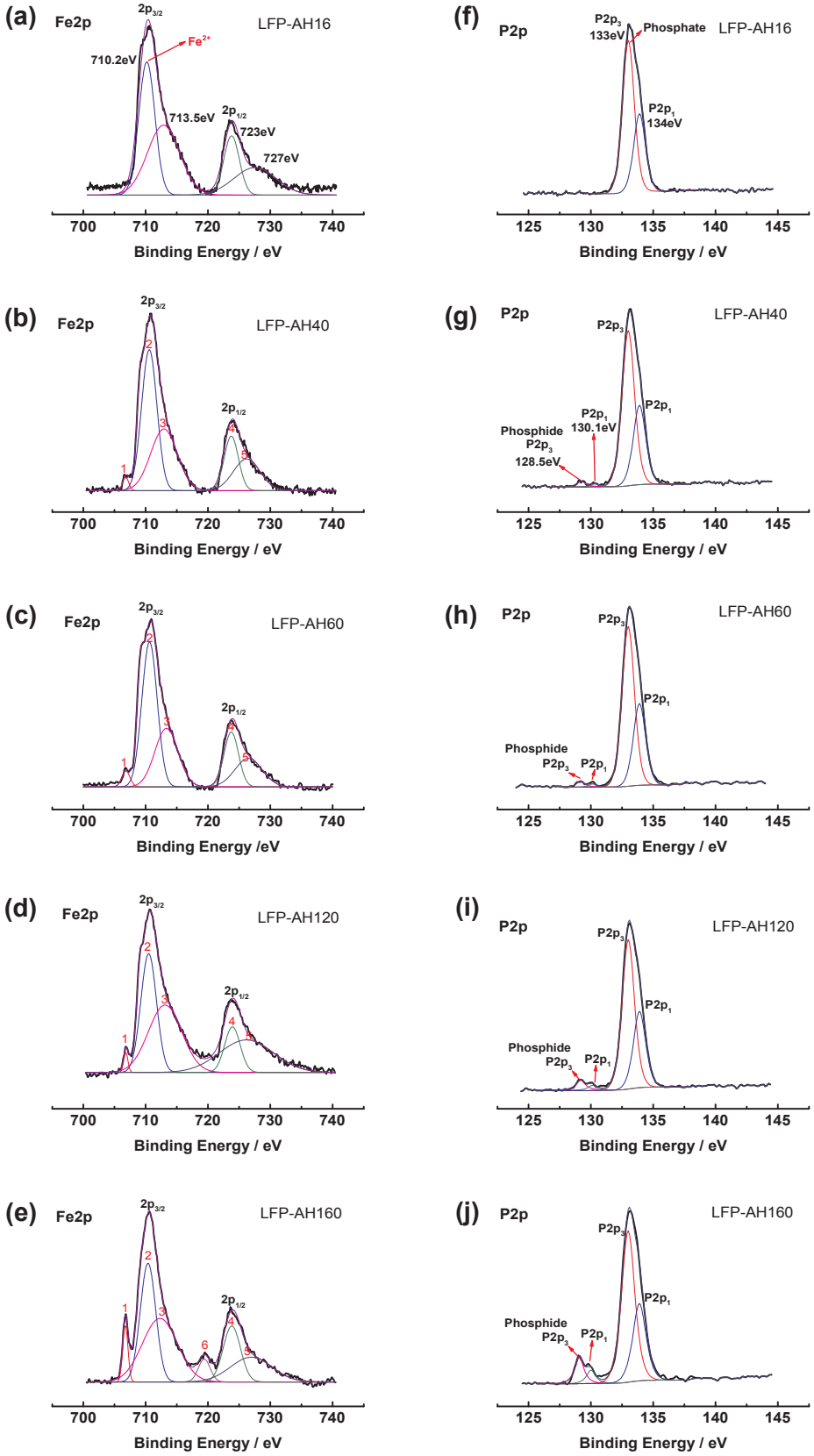

Fig. 5. XPS spectra of Fe2p for (a) LFP-AH16, (b) LFP-AH40, (c) LFP-AH60, (d) LFP-AH120, and (e) LFP-AH160. The XPS spectra of P2p for (f) LFP-AH16, (g) LFP-AH40, (h) LFP-AH60, (i) LFP-AH120, and (j) LFP-AH160.

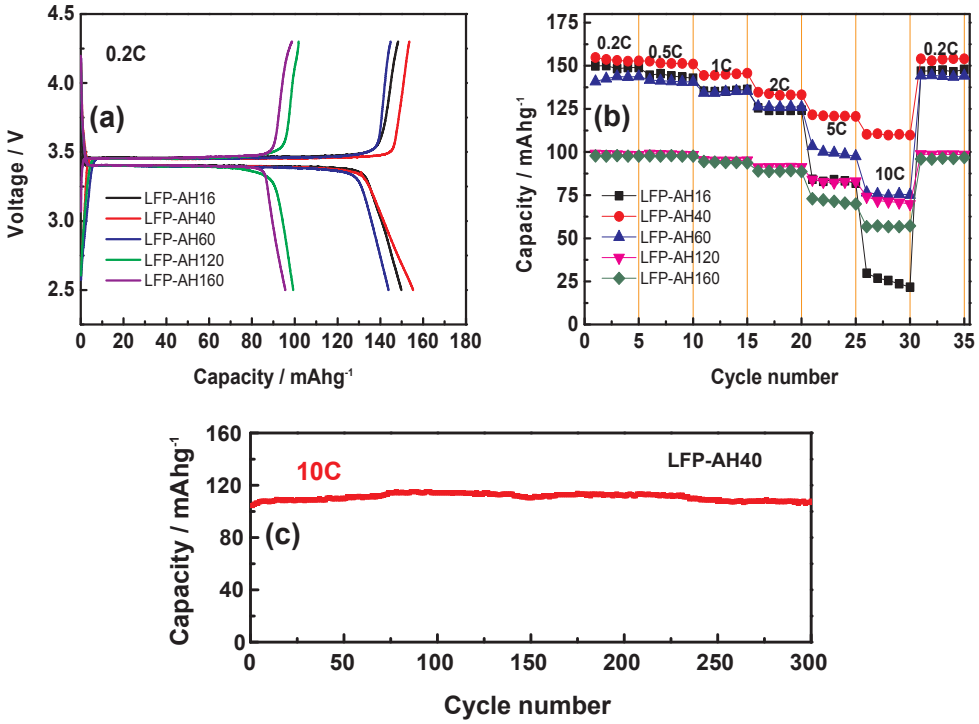

Fig. 6. (a) Charge–discharge profiles of LFP-AH16, LFP-AH40, LFP-AH60, LFP-AH120, and LFP-AH160 at 0.2 C; (b) rate capability of LFP-AH16, LFP-AH40, LFP-AH60, LFP-AH120, and LFP-AH160 at different current densities at room temperature; and (c) long-term cycle performance of LFP-AH40 at 10 C.

comparing these results to those of the other samples, there is no doubt that LFP-AH40 has a better rate performance. It is further suggested that a suitable Fe_2P modification has a favorable effect on improving the rate capability of the $LiFePO_4$ materials, resulting from the effective conductive network provided by Fe_2P. However, the excessive Fe_2P formation on the surface of $LiFePO_4$ is detrimental to the material's electrochemical performance. This outcome is mainly due to the non-electrochemical activity of Fe_2P, which can lead to the specific capacity decrease of the material. As a result, LFP-AH160 exhibits a lower specific capacity than that of pure LFP-AH16. In addition, it was found that LFP-AH160 maintains a good rate performance at a high current density, which is due to the superior conductivity of Fe_2P. Apparently, the introduction of Fe_2P with its excellent electronic conductivity contributes to an enhanced rate capability of the composite material.

As shown above, the enhancement of the material's electrochemical performance is associated with the Fe_2P decoration, which offers abundant channels for electron transfer. To estimate the effect of the conductive improvement on the cycle performance of the sample at a high current, we displayed the long-term cycle life performance of LFP-AH40 at the 10 C charge/discharge rate (Fig. 6(c)). LFP-AH40 has a superior rate performance with a stable cycle. The capacity of the composite electrode shows almost no loss, even after 300 cycles at a 10 C charge/discharge rate, which is similar to the previous experimental results where Fe_2P improved the cycling performance and rate capability [26,27]. The existence of a small amount of Fe_2P on the surface of particles could effectively improve the cycling life of the $LiFePO_4$ material.

The typical impedance spectra of samples LFP-AH16, LFP-AH40, LFP-AH60, LFP-AH120, and LFP-AH160 cycled at 25 °C and 2 C in the fully discharged state are shown in Fig. 7(a). In the figure, a depressed semicircle and a straight line make up the Nyquist plot. The intercept of the depressed semicircle in the high-frequency region is indicative of the surface resistance, which is associated with lithium ion migration through the SEI film (R_{sf}). The depressed semicircle intercept in the medium frequency region directly points to the charge transfer resistance at the solid-film interface (R_{ct}). The straight line in the low frequency region refers to the Warburg impedance. A simulation of the equivalent circuit (inset of Fig. 7(a)) was used to obtain the fitted results of R_s (solution resistance), R_{sf}, and R_{ct} listed in Table 1. Remarkably, the Fe_2P modified samples have lower R_{sf} and R_{ct} values than the pure sample, indicating that the Fe_2P composite introduction favors the decrease of the charge transfer resistance of the material due to its excellent conductivity. However, the R_{sf} and R_{ct} values of the decorated composite gradually become larger with the increasing amount of Fe_2P.

Fig. 7(b) presents the relationship between Z' and $\omega^{-1/2}$ at a low frequency at 25 °C for LFP-AH16, LFP-AH40, LFP-AH60, LFP-AH120, and LFP-AH160. The lithium ion diffusion coefficient (D_{Li}) was obtained using the following theoretical Equations ((1) and (2)):

$$Z' = R_{ct} + R_e + \sigma\omega^{-1/2}, \tag{1}$$

$$D_{Li} = \frac{R^2T^2}{2A^2n^4F^4C_{Li}^2\sigma^2}, \tag{2}$$

where Z' indicates the total resistance of the charge transfer resistance (R_{ct}) and solution resistance (R_e); σ refers to the Warburg factor; ω stands for the angular frequency; R signifies the gas constant; T represents the absolute temperature; n is the number of electrons per molecule during the redox process; and A, F, and C_{Li} denote the surface area of electrode, the Faraday constant, and the concentration of the lithium ion, respectively. The D_{Li} values of LFP-AH16, LFP-AH40, LFP-AH60, LFP-AH120, and LFP-AH160 are shown in Table 1. Compared to the other samples, LFP-AH40 has the highest Li diffusion coefficient, indicating the involvement of a moderate amount of Fe_2P contributes to the improvement of the lithium ion transfer kinetics in the electrode. When the sample is modified by too much Fe_2P, the Li^+ diffusion coefficient of the composite is reduced. Therefore, the superabundant Fe_2P decoration is not conducive to Li^+ transfer.

The magnetization $M(H)$ is the superposition of two contributions, which are the intrinsic part ($\chi_m H$) and extrinsic component (M_{extrin}):

$$M(H) = \chi_m H + M_{extrin};\ M_{extrin} = Nn\mu\zeta(\xi) \tag{3}$$

Here, $\zeta(\xi)$ is the Langevin function, and N is the number of magnetic

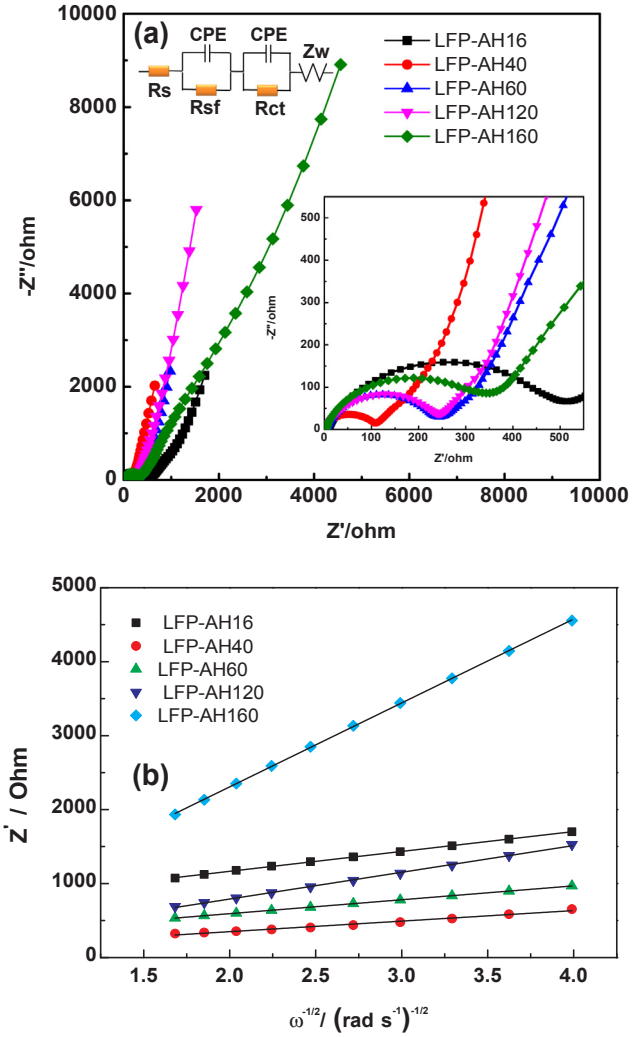

Fig. 7. (a) Typical impedance spectra of LFP-AH16, LFP-AH40, LFP-AH60, LFP-AH120, and LFP-AH160 cycled at 25 °C and 2 C in the fully discharged state; (b) Relationship between Z' and $\omega^{-1/2}$ at the low frequency at 25 °C for LFP-AH16, LFP-AH40, LFP-AH60, LFP-AH120, and LFP-AH160.

Table 1
Values of R_s, R_{sf}, R_{ct}, and D_{Li} for LFP-AH16, LFP-AH40, LFP-AH60, LFP-AH120, and LFP-AH160.

	LFP-AH16	LFP-AH40	LFP-AH60	LFP-AH120	LFP-AH160
R_s	6.73 Ω	2.85 Ω	4.19 Ω	4.5 Ω	4.64 Ω
R_{sf}	3.9 Ω	3.26 Ω	6.85 Ω	10.3 Ω	53.2 Ω
R_{ct}	498.9 Ω	96.81 Ω	249.4 Ω	252.3 Ω	269.4 Ω
D_{Li}	1.38e−14	4.9e−14	2.82e−14	0.76e−14	0.077e−14

clusters. Each cluster is made of n magnetic moments μ. The non-linearity of the $M(H)$ curves is a signature of the ferromagnetic impurities [28,29]. Fig. 8(a) shows the hysteresis curves of LFP-AH16, LFP-AH40, LFP-AH60, LFP-AH120, and LFP-AH160 at 300 K. The hysteresis curves of the other four samples at 300 K are clearly seen in the figure, except for that of LFP-AH16. The hysteresis curve in the present case indicates the existence of ferromagnetism, which results from maghemite (Fe_2P). Moreover, the moment of pure LFP-AH16 is near 0, while the moments of the other 4 samples increase gradually with the increasing reductive gas flow rate, indicating the enhancement of the Fe_2P content. LFP-AH40 displays the best electrochemical performance, which is due to the presence of moderate Fe_2P in the composite material that provides a conductive path for the effective transfer of electrons. However, too much Fe_2P modification has a negative effect on the amelioration of the material's electrochemical performances. On the one hand, lots of Fe_2P generation can sacrifice the specific capacity of the material; On the other hand, it is possible that excessive Fe_2P modification impedes the migration of lithium ion, leading to the degradation of the battery performance. Therefore, it is imperative to eliminate excessive modification. In the reducing gas with 95% Ar and 5% H_2, the magnetic moment of the prepared samples is highly sensitive to the produced magnetic substance (Fe_2P), even though this substance's magnetism is very weak. The magnetization measurement indicates the accurate regulation of the Fe_2P content in the sample can be easily achieved, which means that our approach is an effective method to prepare the optimum $LiFePO_4$ electrode materials. Therefore, it is significant that, by measuring the moment of the $LiFePO_4$ composite material, the optimum *in-situ* Fe_2P surface modification can be sensitively controlled to optimize the material's performance.

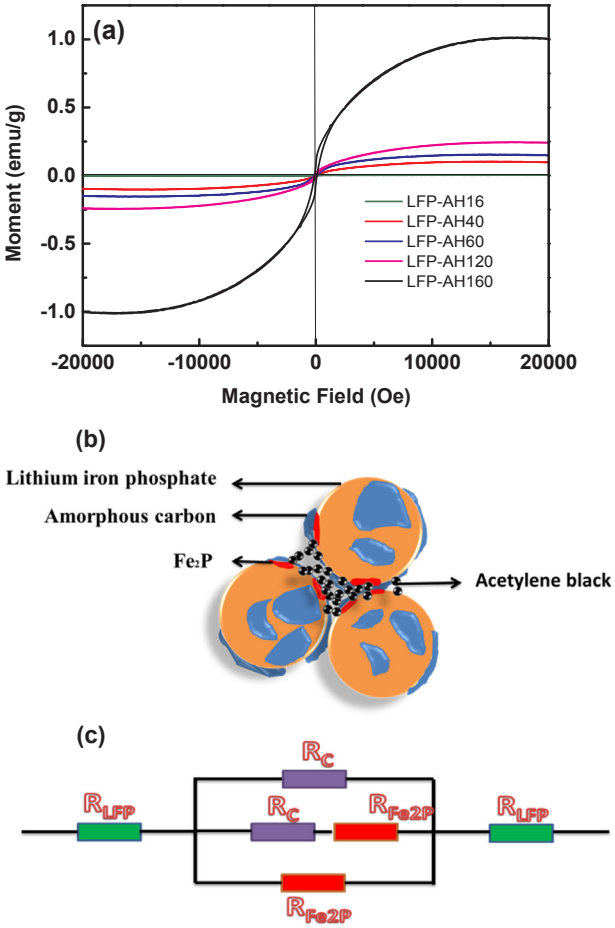

Fig. 8. (a) Hysteresis curves of LFP-AH16, LFP-AH40, LFP-AH60, LFP-AH120, and LFP-AH160 at 300 K; (b) Schematic illustration of the Fe_2P decorated $LiFePO_4$; (c) Phenomenological resistance model image of the composite material modified by Fe_2P. (R_{LFP}, R_C, and R_{Fe2P} are indicative of the $LiFePO_4$ material's resistance, carbon resistance, and Fe_2P resistance, respectively.)

Fig. 8(b) shows the schematic illustration of the Fe_2P decorated $LiFePO_4$. Fig. 4(b) shows that Fe_2P homogeneously appears in the inner surface layer of the $LiFePO_4$ material. The effective electric conductive pathway exists between active particles, contributing to the enhancement of the material's electrochemical performances at a high current density. The introduction of a moderate amount of Fe_2P is beneficial to the transfer kinetics of the lithium ion within the electrode. However, the superabundant Fe_2P in the material's inner surface has a negative impact on the material performance, which is reflected in LFP-AH160's

low specific capacity at a high current density. This is because a large amount of non-electrochemical activity from Fe_2P can sacrifice the specific capacity of the $LiFePO_4$ material. In addition, superabundant Fe_2P decoration may hinder the lithium ion diffusion path, contributing to the poor electrochemical performances. Magnetic measurement is a feasible technology to monitor the growth of Fe_2P within the $LiFePO_4$ material and effectively avoid excessive Fe_2P modification that affects the electrochemical performance of the material. Fig. 8(c) exhibits the phenomenological resistance model image of the composite material modified by Fe_2P. R_{LFP}, R_C, and R_{Fe2P} are indicative of the $LiFePO_4$ material's resistance, carbon resistance, and Fe_2P resistance, respectively. The total resistance relies on the low resistance component in the parallel circuit model. The total resistance of the $LiFePO_4$ composite's value is reduced by the presence of Fe_2P with its low conductivity. This is also a reasonable explanation for the improvement of LFP-AH40.

4. Conclusions

The $LiFePO_4$-Fe_2P composite was prepared by controlling the flow rate of the reductive gas. As confirmed by TEM, the conductive phase of Fe_2P was formed in the inner surface of $LiFePO_4$ due to the common reduction of the reductive gas and carbon coating. In addition, the growth of Fe_2P occurred rapidly as the amount of reductive gas increased. However, not all Fe_2P modification contents are helpful due to its non-electrochemical activity. When the reductive gas flow rate was 40 mL/min, the modified $LiFePO_4$ displayed a higher specific capacity and lower charge transfer resistance, indicating that the introduction of suitable Fe_2P with a high conductivity was beneficial to the establishment of a high-efficiency conductive network. As shown in the experimental results, it is imperative to eliminate excessive Fe_2P modification to further improve the performances of the material. The magnetization was highly sensitive to magnetic substances, and Fe_2P is a ferromagnetic substance, so the accurate regulation of the Fe_2P content in the samples was easily realized by magnetic measurement.

Acknowledgements

The authors wish to acknowledge the financial support by the Natural Science Foundations of China (No. 61574037, 21203025, 11344008, 11204038, 61804030, 11874113), the Natural Science Foundations of Fujian Province of China (2016J01011, 2016J05151). W. Yang would like to thank the support from the project of scientific research of Ningde Normal University (No. 2018Y07) and the major cultivation program of Ningde Normal University (No. 2018ZDK07).

References

[1] Z.G. Yang, Y. Dai, S.P. Wang, J.X. Yu, How to make lithium iron phosphate better: a review exploring classical modification approaches in-depth and proposing future optimization methods, J. Mater. Chem. A 4 (2016) 18210–18222.
[2] N. Paul, J. Wandt, S. Seidlmayer, S. Schebesta, M.J. Mühlbauer, O. Dolotko, H.A. Gasteiger, R. Gilles, Aging behavior of lithium iron phosphate based 18650-type cells studied by in situ neutron diffraction, J. Power Sources 345 (2017) 85–96.
[3] A. Eftekhari, LiFePO4/C nanocomposites for lithium-ion batteries, J. Power Sources 343 (2017) 395–411.
[4] D. Ansean, M. Dubarry, A. Devie, B.Y. Liaw, V.M. García, J.C. Viera, M. Gonzalez, Fast charging technique for high power LiFePO4 batteries: A mechanistic analysis of aging, J. Power Sources 321 (2016) 201–209.
[5] C.L. Gong, Z.G. Xue, S. Wen, Y.S. Ye, X.L. Xie, Advanced carbon materials/olivine LiFePO4 composites cathode for lithium ion batteries, J. Power Sources 318 (2016) 93–112.
[6] Y.B. Guan, J.R. Shen, X.F. Wei, Q.Z. Zhu, X.H. Zheng, S.Q. Zhou, B. Xu, LiFePO4/activated carbon/graphene composite with capacitive-battery characteristics for superior high-rate lithium-ion storage, Electrochim. Acta 294 (2019) 148–155.
[7] Y.S. Hu, P. Guo, J. Thompson, Z.H. Wang, Rational design of mesoporous LiFePO4@C nanofibers as cathode materials for energy storage, Ceram. Int. 43 (2017) 10201–10206.
[8] A. KumarBudumuru, M. Viji, A. Jena, B.R.K. Nanda, C. Sudakar, Mn substitution controlled Li-diffusion in single crystalline nanotubular LiFePO4 high rate-capability cathodes: experimental and theoretical studies, J. Power Sources 406 (2018) 50–62.
[9] S.S. Jiang, Y.S. Wang, Synthesis and characterization of vanadium-doped LiFePO4@C electrode with excellent rate capability for lithium-ion batteries, Solid State Ionics 335 (2019) 97–102.
[10] Y.-H. Rho, L.F. Nazar, L. Perry, D. Ryan, Surface chemistry of LiFePO4 studied by mössbauer and X-ray photoelectron spectroscopy and its effect on electrochemical properties, J. Electrochem. Soc. 154 (2007) A283–A289.
[11] Y. Lin, M.X. Gao, D. Zhu, Y.F. Liu, H.G. Pan, Effects of carbon coating and iron phosphides on the electrochemical properties of LiFePO4/C, J. Power Sources 184 (2008) 444–448.
[12] Y.H. Yin, M.X. Gao, H.G. Pan, L.K. Shen, X. Ye, Y.F. Liu, P.S. Fedkiw, X.W. Zhang, High-rate capability of LiFePO4 cathode materials containing Fe2P and trace carbon, J. Power Sources 199 (2012) 256–262.
[13] L.Y. Zhang, Y.F. Tang, Z.Q. Liu, H.N. Huang, Y.Z. Fang, F.Q. Huang, Synthesis of Fe2P coated LiFePO4 nanorods with enhanced Li-storage performance, J. Alloys and Compounds 627 (2015) 132–135.
[14] M. Mokhlesur Rahman, J.-Z. Wang, R. Zeng, D. Wexler, H.K. Liu, LiFePO4-Fe2P-C composite cathode: An environmentally friendly promising electrode material for lithium-ion battery, J. Power Sources 206 (2012) 259–266.
[15] K.S. Dhindsa, A. Kumar, G.A. Nazri, V.M. Naik, V.K. Garg, A.C. Oliveira, P.P. Vaishnava, Z.X. Zhou, R. Naik, Enhanced electrochemical performance of LiFePO4/C nanocomposites due to in situ formation of Fe2P impurities, J. Solid State Electrochem. 2 (2016) 2275–2282.
[16] W. Chang, S. Kim, I. Park, B. Cho, K. Chung, H. Shin, Low temperature performance of LiFePO4 cathode material for Li-ion batteries, J. Alloys and Compounds 563 (2013) 249–253.
[17] C.W. Kim, J.S. Park, K.S. Lee, Effect of Fe2P on the electron conductivity and electrochemical performance of LiFePO4 synthesized by mechanical alloying using Fe3+ raw material, J. Power Sources 163 (2006) 144–150.
[18] Y.J. Qiu, Y.H. Geng, J. Yu, X.B. Zuo, High-capacity cathode for lithium-ion battery from LiFePO4/(C+Fe2P) composite nanofibers by electrospinning, J. Mater. Sci. 49 (2014) 504–509.
[19] P.S. Herle, B. Ellis, N. Coombs, L.F. Nazar, Nano-network electronic conduction in iron and nickel olivine phosphates, Nat. Mater. 3 (2004) 147–152.
[20] K.T. Lee, K.S. Lee, Electrochemical properties of LiFe0.9Mn0.1PO4/Fe2P cathode material by mechanical alloying, J. Power Sources 189 (2009) 435–439.
[21] A. Yamada, S.C. Chung, K. Hinokuma, Optimized LiFePO4 for lithium battery cathodes, J. Electrochem. Soc. 148 (2001) A224–A229.
[22] N. Ravet, Y. Chouinard, J.F. Magnan, S. Besner, M. Gauthier, M. Armand, Electroactivity of natural and synthetic triphylite, J. Power Sources 98 (2001) 503–507.
[23] Z. Wu, W. Ren, L. Xu, F. Li, H. Cheng, Doped graphene sheets as anode materials with super high rate and large capacity for lithium ion batteries, ACS Nano 5 (2011) 5463–5471.
[24] M. Talebi Esfandarani, O. Savadogo, Enhancement of electrochemical properties of platinum doped LiFePO4/C cathode material synthesized using hydrothermal method, Solid State Ionics 261 (2014) 81–86.
[25] R. Dedryvere, M. Maccario, L. Croguennec, F. Le Cras, C. Delmas, D. Gonbeau, X-Ray photoelectron spectroscopy investigations of carbon-coated LixFePO4 materials, Chem. Mater. 20 (2008) 7164–7170.
[26] M. Konarova, I. Taniguchi, Physical and electrochemical properties of LiFePO4 nanoparticles synthesized by a combination of spray pyrolysis with wet ball-milling, J. Power Sources 194 (2009) 1029–1035.
[27] Y. Kadoma, J.-M. Kim, K. Abiko, K. Ohtsuki, K. Ui, N. Kumagai, Optimization of electrochemical properties of LiFePO4/C prepared by an aqueous solution method using sucrose, Electrochim. Acta 55 (2010) 1034–1041.
[28] A. Ait-Salah, A. Mauger, C.M. Julien, F. Gendron, Nano-sized impurity phases in relation to the mode of preparation of LiFePO4, Mater. Sci. Eng. B 129 (2006) 232–244.
[29] K. Zaghib, N. Ravet, M. Gauthier, F. Gendron, A. Mauger, J.B. Goodenough, C.M. Julien, J. Power Sources 163 (2006) 560–566.